Unstable vortex flow and new inertia-driven vortex rolls resulting from an air jet impinging onto a confined heated horizontal disk

F.C. Hsieh, J.H. Wu, J.C. Hsieh, T.F. Lin *

Department of Mechanical Engineering, National Chiao Tung University, Hsinchu 30010, Taiwan, ROC

Abstract

An experiment combining flow visualization and temperature measurement is carried out here to investigate the possible presence of new inertia-driven vortex rolls and some unique characteristics of the time-dependent mixed convective vortex flow in a high-speed round air jet impinging onto a heated horizontal circular disk confined in a vertical cylindrical chamber. How the jet Reynolds and Rayleigh numbers and jet-to-disk separation distance affect the unique vortex flow characteristics is examined in detail. Specifically, the experiment is conducted for the jet Reynolds number varying from 0 to 1623 and Rayleigh number from 0 to 63,420 for the jet-to-disk separation distance fixed at 10.0, 20.0 and 30.0 mm. The results indicate that at sufficiently high Re_j the inertia-driven tertiary and quaternary rolls can be induced aside from the primary and secondary rolls. At an even higher Re_j the vortex flow becomes unstable due to the inertia-driven flow instability. Only for $H = 20.0$ mm the flow is also subjected to the buoyancy-driven instability for the ranges of the parameters covered here. Because of the simultaneous presence of the inertia- and buoyancy-driven flow instabilities, a reverse flow transition can take place in the chamber with $H = 20.0$ mm. At the large H of 30.0 mm the flow unsteadiness results from the mutual pushing and squeezing of the inertia- and buoyancy-driven rolls since they are relatively large and contact with each other. It is also noted that the critical Re_j for the onset of unsteady flow increases with ΔT for $H = 10.0$ and 20.0 mm. But for $H = 30.0$ mm the opposite is true and raising ΔT can destabilize the vortex flow. Based on the present data, flow regime maps delineating the temporal state of the flow are provided and correlating equations for the boundaries separating various flow regimes are proposed.
© 2006 Elsevier Ltd. All rights reserved.

1. Introduction

Recent intensive investigation on the flow and heat transfer associated with a jet impinging onto a large heated flat plate has been mainly its superior heat transfer capability. The advantage of the highly efficient jet impinging cooling has been applied to many technological processes such as the drying of textiles and paper products, annealing of glass, cooling of gas turbine components and microelectronic equipments, freezing of tissue in cryosurgery, etc. [1]. In the microelectronic fabrication industry low speed impinging jets are often employed in the growing semiconductor thin crystal films on heated silicon wafers through rapid

thermal processing (RTP) [2] and chemical vapor deposition (CVD) processes [3]. In order to obtain high-quality thin films, the flow in the CVD chamber needs to be stable and contains no vortices. Thus the detailed understanding of the vortex flow characteristics in the low speed impinging jet flow are rather important in the thin crystal film growth. In the present study, we intend to unveil some unique characteristics of the mixed convection unstable vortex flow in a jet impinging vertically downwards onto a horizontal heated plate. Particularly, the vortex flow instability driven by the inertia and buoyancy will be examined in detail.

Considerable research has been carried out in the past to study the heat transfer and fluid flow in a round or slot jet impinging onto a horizontal plate. Most of existing studies relevant to the impinging jets deal with heat and mass transfer of a single jet impinging onto a flat plate, emphasizing the high heat transfer efficiency of the jet. For instances,

---

* Corresponding author. Tel.: +886 35 712121 55118; fax: +886 35 726440.
E-mail address: tflin@mail.nctu.edu.tw (T.F. Lin).

Nomenclature

D_j	diameter of jet at the pipe exit (mm)
f	main oscillation frequency (Hz)
Gr	Grashof number, $g\beta\Delta TH^3/v^2$
g	gravitational acceleration (m/s^2)
H	distance between the exit of injection pipe and heated plate (mm)
Q_j	jet flow rate (standard liter per minute, slpm)
r, θ, z	dimensional coordinate system of cylinder (mm)
R, Θ, Z	dimensionless coordinate system of cylinder, r/R_c, $\theta/360°$, z/H
Ra	Rayleigh number, $g\beta\Delta TH^3/\alpha v$
Re_j	Reynolds number of injection, $\overline{V_j}D_j/v$
t	time instant (s)
T_f	temperature of the heated disk (°C)

T_j	temperature of injected air jet (°C)
V_j	velocity of the air jet at the injection pipe exit (m/s)
$\overline{V_j}$	average speed of the air jet at the injection pipe exit (m/s)

Greek symbols

α	thermal diffusivity (cm^2/s)
β	thermal expansion coefficient (K^{-1})
ΔT	temperature difference between the heated disk and the air injected (°C)
μ	coefficient of viscosity (N m/m^2)
v	kinematic viscosity (m^2/s)
Φ	non-dimensional temperature, $(T - T_j)/(T_f - T_j)$

heat or mass transfer in the laminar and turbulent imping-ing jets was experimentally investigated by Scholtz and Trass [4], Sparrow and Wong [5], Masliyah and Nguyen [6], and Hrycak [7]. Moreover, the laminar impinging jets with an upper plate confinement were numerically predicted by Saad et al. [8] and Law and Masliyah [9].

The presence of a confinement plate in jet impingement was noted to induce a complicated flow around the jet axis [10,11]. The recirculating flow resulting from a confined impinging gas jet at low Re_j was visualized by Santen et al. [12,13], Cheng et al. [14] and Hsieh et al. [15]. It has been noted that the flow of impinging jet can become unstable as the Rayleigh number exceeds certain critical level. This is known as the buoyancy-driven flow instabil-ity. Furthermore, Santen et al. [12,13] explained the sup-pression of the buoyancy-induced flow at increasing jet Reynolds numbers. Hsieh et al. [15] reported that the flow recirculation consisted of three circular vortex rolls includ-ing a primary inertia-driven vortex roll around the jet, a secondary inertia-driven vortex roll in the middle region, and a buoyancy-induced vortex roll in the outer zone. The inner and middle vortex rolls are driven by the viscous shear due to a non-uniform velocity distribution in the jet and are stronger and bigger at a high Re_j. But the buoy-ancy-driven outer vortex roll is important at high buoy-ancy-to-inertia ratio. The secondary inertia-driven vortex roll only appears at certain high Re_j and is much smaller and weaker than the primary inertia-driven vortex roll. Cheng et al. [14] indicated that increasing the chamber pressure and/or the temperature difference between the heated plate and air jet caused the outer roll to become lar-ger and the inner roll to become correspondingly smaller. Hsieh et al. [15] showed that the vortex flow became time periodic at a certain high buoyancy-to-inertia ratio and the oscillation frequency of the vortex flow increased with Re_j. More recently, Chung and Luo [16] and Chiriac and Ortega [17] demonstrated that heat transfer rate along the target plate was enhanced by an unsteady impinging

jet. As the Reynolds number exceeding certain critical level, a steady to unsteady flow pattern transition for a confined laminar impinging jet with $Re_j < 1000$ was numerically investigated by Chiriac and Ortega [17]. They also indi-cated that the critical jet Reynolds number for the onset of unsteady flow was between 585 and 610. Moreover, the dominant frequency of the unsteady jet flow is in accor-dance with the primary vortices emanating from the shear layer produced by the jet just issued from the nozzle. The transition between the laminar and turbulent impinging jet flow at $Re_j = 1500$ was suggested by Elison and Webb [18]. A combined experimental and numerical study was carried out by Narayanan et al. [19] to study an impinging slot jet flow. They noted that the secondary peak in the heat transfer coefficient was still high owing to the interac-tion between the streamwise velocity variance and related motion in the outer region and to the near-wall turbulence. Critical review on various aspects of the flow and heat transfer associated with the impinging jets has been con-ducted by Viskanta [20] and Jambunathan et al. [21].

The above literature review clearly reveals that various aspects of the flow and heat transfer associated with the iner-tia dominated high-speed impinging jets have been exten-sively investigated. However, the complex flow structures and the associated thermal characteristics for the impinging jets simultaneously driven by the jet inertia and buoyancy remain poorly understood. In an initial attempt to investi-gate this mixed convective vortex flow, we [15] recently car-ried out an experimental study to delineate the steady and time periodic vortex flow patterns resulting from a vertically downward air jet impinging onto a horizontal heated disk confined in a vertical cylindrical chamber. For the ranges of parameters covered there for Q_j and ΔT respectively varied from 0 to 5.0 slpm (standard liter per minute) and 0 to 25.0 °C at the jet-to-disk separation distance $H = 20.0$ mm, the vortex flow was found to be mainly composed of two inertia-driven circular rolls and a buoyancy-driven circular rolls. At a high buoyancy-to-inertia ratio new rolls

are generated and the flow becomes time-dependent. Over a certain range of the buoyancy-to-inertia ratio, a cyclic process characterized by the generation, growth, decay and disappearance of the new rolls prevails and the flow is time periodic. The time-dependent flow is driven by the buoyancy. Recently, an inertia-driven tertiary roll induced at certain higher Re_j and the effects of the jet-to-disk separation distance on the vortex flow characteristics were reported by Hsieh and Lin [22]. In this continuing study we re-conduct the experiment of Hsieh et al. [15] for H ranging from 10.0 to 30.0 mm over a wider range of the jet flow rate, intending to explore the possible presence of new forms of time-dependent vortex flow and reverse flow transition at increasing buoyancy. Besides, the possible appearance of a quaternary roll at even higher Re_j will be examined. Attention will be focused on the conditions leading to these new vortex flows and on the characteristics of these flows.

2. Experimental apparatus and procedures

The experimental system established in our previous study [15] is also employed here to investigate the unstable vortex flow characteristics associated with a round air jet impinging vertically downwards onto a circular horizontal heated disk confined in a vertical cylindrical chamber.

Schematics of the experimental system and test section are respectively shown in Figs. 1 and 2. The system consists of four major parts – the processing chamber, temperature measurement and data acquisition unit, heating unit, and gas injection unit. The major parts are briefly described in the following.

The processing chamber is made of 6.0-mm thick quartz glass to allow for the observation of the vortex flow in it. The chamber is cylindrical and has an inside diameter of 291.0 mm and the height of the cylindrical chamber is 200.0 mm. To facilitate the flow visualization, the chamber top is made of an acrylic plate. Air is injected vertically downwards from a long straight circular pipe into the cylindrical chamber along the axis of the chamber and impinges directly onto the heated disk. The air first flows over the heated disk, then moves through the annular section of the chamber, and finally leaves the chamber via 20 circular outlets of 12.7 mm in diameter opened at the bottom of the chamber. The chamber is sealed to prevent any gas leakage. The top, bottom and side walls of the chamber are thermally well insulated to reduce the heat loss from the processing chamber to the ambient by covering the entire chamber with a superlon insulator of 100.0 mm thick. The insulator can be opened during the flow visualization.

The heating unit is designed to maintain the circular disk at the preset uniform temperature during the experiment. It is composed of a 25.0-mm thick high purity circular copper plate of 8-in. in diameter, acting as the disk. The heater attached onto the back side of the copper plate is divided into three concentric zones. Each zone is independently heated by a DC power supply with DC current passing through the nickel coil placed on a stainless steel base.

To reduce the heat loss from the sidewall of the copper plate and stainless steel base, the lateral surface of the entire heating unit is wrapped with a 16-mm thick thermal insulation layer of superlon. Care is taken to insure that the outside surface of the insulation layer is smooth and cylindrical. The entire heating unit is then placed on a Teflon plate. A proper control of the voltage from each power supply allows us to maintain the copper plate at a nearly uniform temperature. The measured data indicate that the uncertainty in maintaining the copper plate temperature is ±0.1 °C. No bias in the plate temperature is noted and the temperature non-uniformity is spatially random.

The gas injection unit consists of a 2HP air compressor, a flow meter, a smoke generator, filters, pressure regulator, and connection and injection pipes. In the experiments, air is drawn from the ambient by the compressor and sent into a 300-l and 100-psi high-pressure air tank and it is filtered to remove moisture and tiny particles. The installation of the high-pressure air tank intends to suppress the fluctuation of the air flow and extends the life of the compressor. Then, the air is mixed with smoke tracers in the smoke generator and regulated by the pressure regulator, and is later injected into the processing chamber through the straight circular injection pipe which is coaxial with the processing chamber. The downward vertical air jet issuing from the pipe exit impinges directly onto the heated plate. In the present study, an injection pipe with diameter 10.0 mm is chosen and the straight portion of the pipe is 600.0-mm long. This length of the injection pipe is selected to ensure that they are long enough for the flow to become fully developed in the pipe. The separation distance between the exit of the injection pipe and the heated disk is fixed at 10.0, 20.0 and 30.0 mm. The air temperature at 600.0-mm upstream of the exit of the injection pipe is measured by a corrected and calibrated T-type thermocouple. The measured value is considered as the temperature of the air injected into the processing chamber since the whole injection pipe is thermally well insulated by a 16.0-mm layer of superlon insulation.

A smoke-tracer flow visualization technique is employed to observe the flow patterns in the cylindrical chamber. The gas flow pattern is illuminated by the vertical and horizontal plane light sheets produced by passing parallel light sheets from an overhead projector through adjustable knife edges. The experimental system is located in a darkroom to improve the contrast of the flow photos. The time variations of the flow pattern during the entire transient stage from the top and side views are recorded by the Sony digital video camera DCR-PC100. The recorded images are later examined carefully in a personal computer. The air temperature in the processing chamber is measured by inserting a small thermocouple probe into the chamber through small holes of 1.0 mm in diameter opened at the top of the chamber. The probe is an OMEGA (model HYPO) mini hypodermic extremely small T-type thermocouple implanted in a 1-in. long stainless steel hypodermic needle.
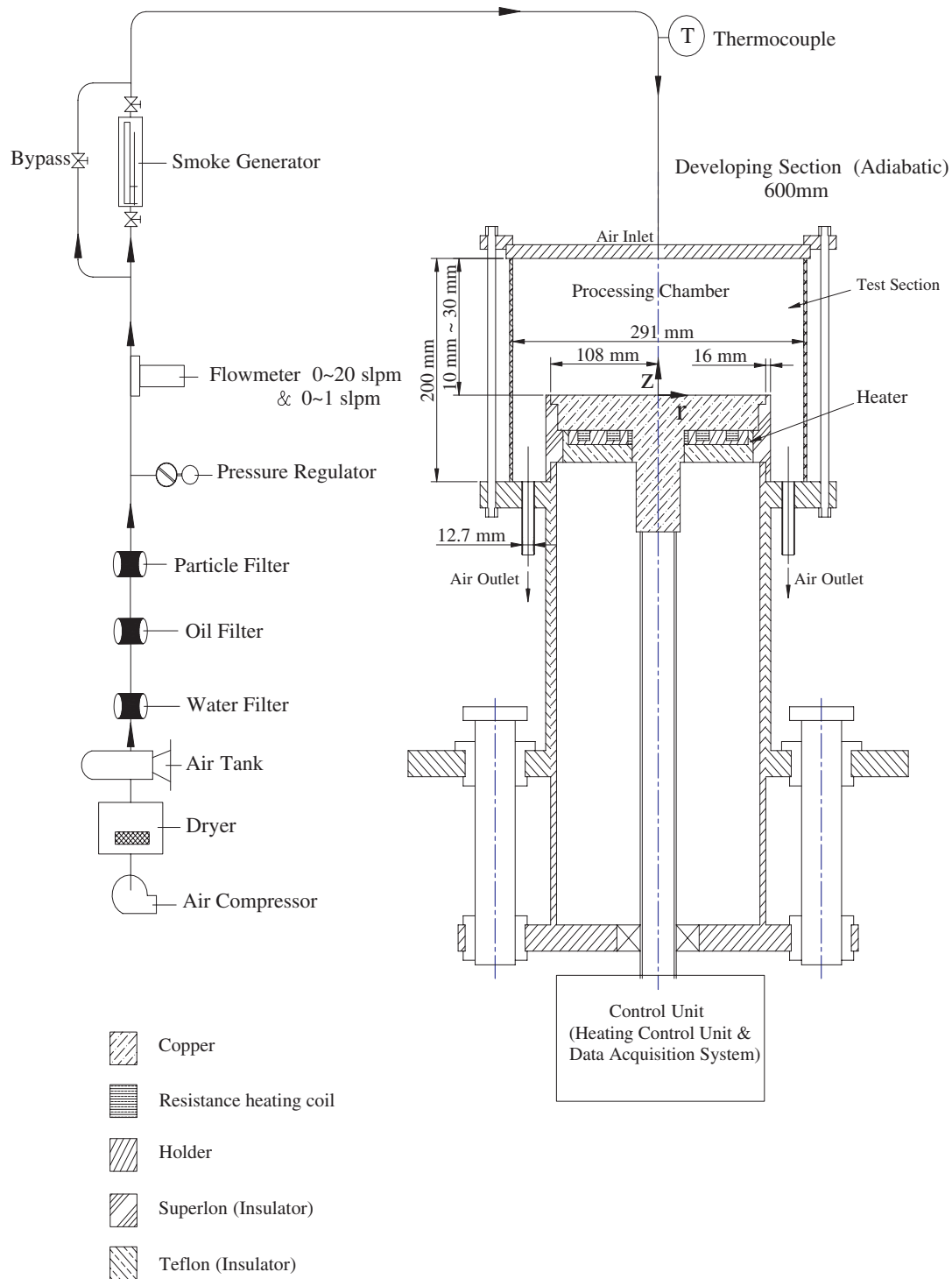
Fig. 1. Schematic diagram of the experimental system.

For each case the experiment starts with the air at the room temperature compressed first into the smoke generator through the connection pipe and then injected into the processing chamber. The air moves over the heated disk and finally leaves the chamber through the outlets at the bottom of the chamber. In the meantime the temperature of the disk and the air flow rate are controlled at the preset levels. As the mixed convective air flow in the processing chamber reaches steady or statistically stable state, we begin to visualize the vortex flow pattern in the chamber.

Uncertainties in the Rayleigh number, Reynolds number and other independent parameters are calculated according to the standard procedures established by Kline and McClintock [23]. The uncertainties of the thermophysical properties of the air are also included in the analysis. The fundamental thermophysical properties of the working
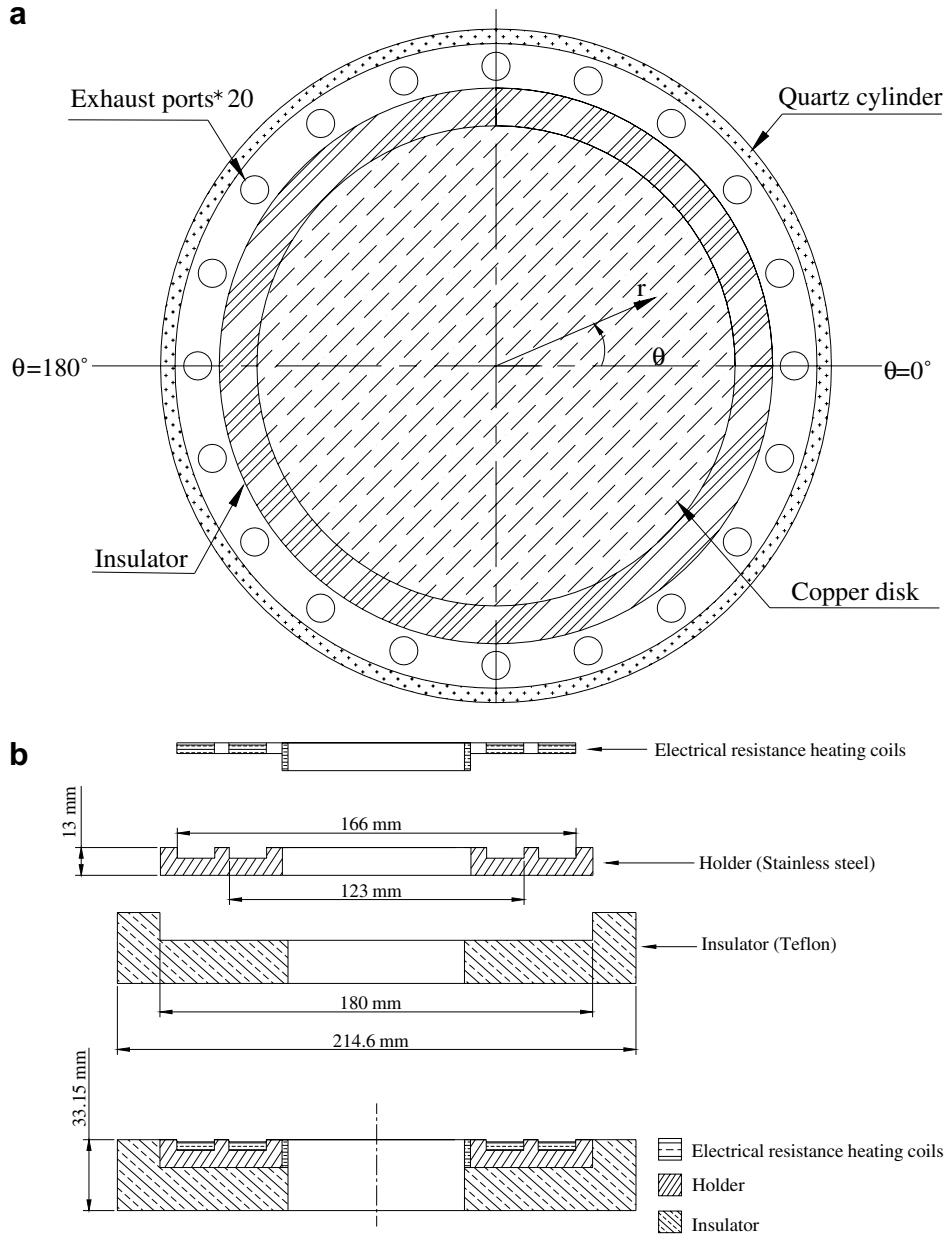
a

b

Fig. 2. Schematic of (a) the test section from the top view and (b) 3-zone concentric heater.

fluid (air) are $\alpha = 0.22$ (cm^2/s), $\beta = 0.0034$ (K^{-1}), $v = 0.16$ (cm^2/s) and $Pr = 0.72$ at 30 °C and 1.0 bar. In addition, the uncertainties of the control unsteadiness and temperature non-uniformity are accounted for in the evaluation of the data uncertainty. The analysis shows that the uncertainties of temperature, volume flow rate, dimensions, Reynolds number, and Rayleigh number measurements are estimated to be less than ± 0.2 °C, $\pm 2\%$, ± 0.05 mm, 2.3% and 8.6%, respectively.

3. Results and discussion

In the present experiment the air flow rate Q_j is varied from 0 to 12.0 slpm and the temperature difference between the heated disk and injection air ΔT is varied from 0 to

25.0 °C for three jet-to-disk separation distances with $H = 10.0$, 20.0 and 30.0 mm at the injection pipe diameter $D_j = 10.0$ mm. The dimensionless groups governing the flow are the jet Reynolds number and the Rayleigh number, and the ratio of the jet-to-disk separation distance to pipe diameter. They are respectively defined as

$$Re_j = \frac{V_j D_j}{v} = \frac{4}{\pi} \frac{Q_j}{v D_j}, \qquad (1)$$

$$Ra = \frac{g \beta \Delta T H^3}{\alpha v}, \qquad (2)$$

and

$$A = \frac{H}{D_j} \qquad (3)$$

Thus in this study Re_j and Ra range respectively from 0 to 1623 and 0 to 63,420 and A varies from 1.0 to 3.0. In what follows selected flow photos from the top and side views are examined closely to illustrate the possible existence of new vortex rolls and new time-dependent vortex flow patterns. Besides, the conditions leading to these new vortex flow structures and their characteristics affected by the governing diameters resulting from the air impinging jet in the processing chamber will be addressed.

3.1. Inertia-driven tertiary and quaternary rolls and onset of unsteady flow

To illustrate the presence of new vortex rolls, the typical steady vortex flow patterns driven at certain high jet Reynolds numbers observed in the cylindrical chamber for the jet-to-disk separation distance at $H = 20.0$ and 10.0 mm are shown in Fig. 3. The steady flow photos from the side view are shown along with the corresponding sche-

matically sketched vortex flow patterns to indicate the actual direction of the flow recirculation, which is based on the detailed flow visualization. The flow is axisymmetric at these low buoyancy-to-inertia ratios with $H = 20.0$ mm ($Re_j = 784$, $Ra = 3760$ and $Gr/Re_j^2 = 8.74 \times 10^{-3}$) and $H = 10.0$ mm ($Re_j = 1150$, $Ra = 470$ and $Gr/Re_j^2 = 5.08 \times 10^{-4}$), and only the side view flow photos at the vertical plane $\theta = 0°$ are given here. The results in Fig. 3(a) indicate that at $Re_j = 784$ four circular vortex rolls are induced in the chamber for $H = 20.0$ mm, namely, the three inertia-driven and one buoyancy-driven rolls. Detailed information on the characteristics of the observed primary inertia-driven roll, secondary inertia-driven roll and buoyancy-driven roll from the confined impinging gas jet are already available from our previous study [15] and is not repeated here. The small tertiary circular roll can be seen in the region above the large primary inertia-driven inner roll and adjacent to the chamber top and is found to be induced through the viscous shearing effects produced by
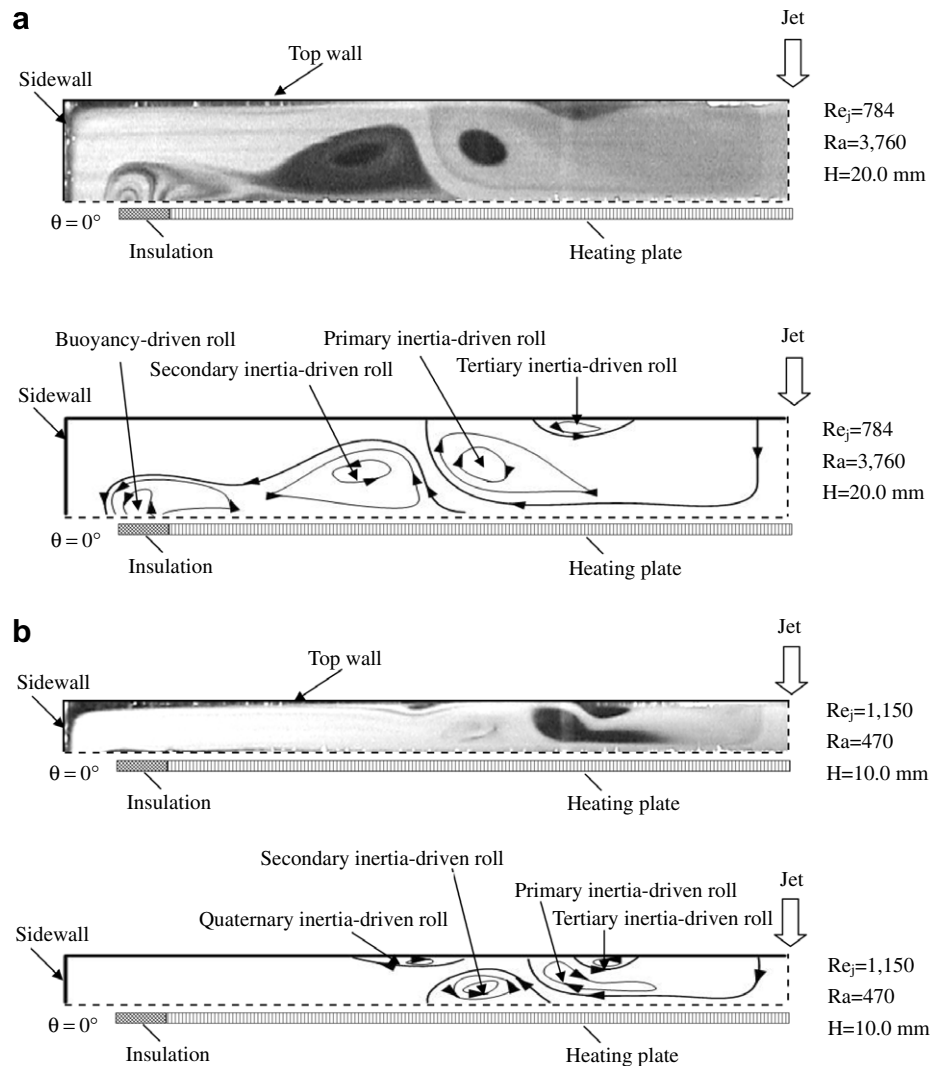

Fig. 3. Steady side view flow photo taken at the vertical plane $\theta = 0°$ and the corresponding schematically sketched cross plane vortex flow for (a) $H = 20.0$ mm for $Re_j = 784$ ($Q_j = 5.8$ slpm) and $Ra = 3760$ ($\Delta T = 5.0$ °C), and (b) $H = 10.0$ mm for $Re_j = 1150$ ($Q_j = 8.5$ slpm) and $Ra = 3760$ ($\Delta T = 5.0$ °C).

the strong inner vortex roll at high Re_j. The tertiary roll was first unveiled in our recent study [22]. We further note from the results in Fig. 3(b) for $H = 10.0$ mm that four circular vortex rolls are also induced in the chamber at the much higher Re_j of 1150. Since the buoyancy-to-inertia ratio is relatively low at this Re_j, no buoyancy-driven roll is induced. More specifically, in addition to the primary, secondary and tertiary inertia-driven rolls, a quaternary roll appears near the top of the chamber. This roll is small and weak and found to result also from viscous shearing effects produced by the relatively strong inertia-driven secondary vortex roll at this high Re_j, which is termed as the quaternary inertia-driven roll. Moreover, our data show that at $H = 10.0$ mm the quaternary inertia-driven roll is induced only when the jet Reynolds number exceeds certain level around 1014 for the unheated disk with $Ra = 0$. Besides, a higher Re_j is needed for the onset of the tertiary inertia-driven roll in the chamber with the smaller H of 10.0 mm ($Re_j = 744$ at $Ra = 0$) when compared with that for $H = 20.0$ mm.

The critical conditions for the appearance of the tertiary and quaternary inertia-driven vortex rolls and the unsteady flow in the chamber under the action of buoyancy are of interest in the fundamental fluid flow study and technological applications. Some results for these critical conditions for the unheated disk ($Ra = 0$) are reported in the previous study [22]. The onsets of the inertia-driven new vortex rolls and inertia-driven time-dependent flow are ascertained by carefully visualizing the flow in the processing chamber at increasing jet Reynolds number [22]. The present results suggest that as the jet Reynolds number exceeds certain higher levels the tertiary and quaternary inertia-driven vortex rolls and the inertia-driven time-dependent flow appear.

More specifically, at increasing jet Reynolds number for given H and ΔT the primary, secondary, tertiary and the quaternary inertia-driven rolls appear in sequence, as evident from the data summarized in Table 1. So the quaternary inertia-driven roll is initiated at a higher Reynolds number than the other rolls. For a higher ΔT a higher Re_j is required to initiate the tertiary or quaternary roll. When the jet-to-disk separation distance is reduced, we also need a higher Re_j to initiate the inertia-driven rolls. It should be mentioned that for the range of the parameters covered here the quaternary inertia-driven roll does not appear at $H = 20.0$ and 30.0 mm. Besides, at $H = 30.0$ mm the tertiary inertia-driven roll only appears when $\Delta T = 0\,°C$.

The present data for the critical Re_j for the onset of the inertia-driven time-dependent flow for various H and ΔT are summarized in Table 2. Note that the critical Re_j increases slightly with ΔT for $H = 10.0$ and 20.0 mm. While for the higher H of 30.0 mm an opposite trend is noted. This opposite trend results from the fact that for $H = 30.0$ mm at given Q_j and ΔT, the inertia- and buoyancy-driven rolls are both large and in close contact, as reported in the previous study [22]. An increase in ΔT first causes the buoyancy-driven roll to grow, which in turn squeezes the inertia-driven roll. Then the inertia-driven roll pushes back. These two mechanisms result in the cyclic growth and decay of the two rolls and the vortex flow becomes unsteady. For a higher ΔT the buoyancy roll is bigger and the inertia-driven roll starts to push the bigger buoyancy roll at a lower Re_j. Thus at the higher H of 30.0 mm the critical Re_j is lower for a higher ΔT. While for the smaller H of 10.0 and 20.0 mm the inertia- and buoyancy-driven rolls are much smaller. They are not in

Table 1
Critical condition for appearance of the tertiary and quaternary inertia-driven roll

Vortex roll	Separation distance (H, mm)	ΔT (°C)	Flow rate (Q_j, slpm)	Re_j	Ra	$(Gr/Re_j^2) \times 10^{-3}$
Tertiary inertia-driven roll	10.0	0	5.5	744	0	0
		5.0	5.6	757	470	1.17
		10.0	5.8	784	940	2.18
		15.0	6.0	811	1410	3.06
		20.0	6.2	839	1880	3.81
		25.0	6.4	866	2350	4.48
	20.0	0	5.0	676	0	0
		5.0	5.2	703	3760	10.9
		10.0	5.4	730	7520	20.0
		15.0	5.6	757	11,270	28.1
		20.0	5.8	784	15,030	34.9
		25.0	6.0	811	18,790	40.8
	30.0	0	4.6	622	0	0
Quaternary inertia-driven roll	10.0	0	7.5	1014	0	0
		5.0	7.8	1055	470	0.602
		10.0	8.0	1082	940	1.14
		15.0	8.2	1109	1410	1.63
		20.0	8.4	1136	1880	2.08
		25.0	8.6	1163	2350	2.48

Table 2
Critical condition for the onset of the time periodic flow for various H

Separation distance (H, mm)	ΔT (°C)	Flow rate (Q_j, slpm)	Re_j	Ra	$(Gr/Re_j^2) \times 10^{-3}$
10.0	0	7.7	1041	0	0
	5.0	8.6	1163	470	0.495
	10.0	8.6	1163	940	0.99
	15.0	8.7	1177	1410	1.45
	20.0	9.0	1217	1880	1.81
	25.0	9.3	1258	2350	2.12
20.0	0	5.9	798	0	0
	5.0	6.2	839	3760	7.63
	10.0	6.6	893	7520	13.5
	15.0	6.9	933	11,270	18.5
	20.0	7.2	974	15,030	22.6
	25.0	7.3	987	18,798	27.6
30.0	0	5.9	798	0	0
	5.0	5.7	774	12,680	30.2
	10.0	5.5	744	25,370	65.5
	15.0	5.0	676	38,050	119
	20.0	4.5	609	50,730	195
	25.0	3.5	473	63,420	405

close contact and the squeezing and pushing mechanisms between the rolls do not exist. It is of interest to note that the onset condition of the circumferential rotation of the deformed vortex rolls is the same as that for the onset of inertia-driven time-dependent flow given in Table 2. But at $H = 10.0$ mm the deformed vortex rolls do not rotate circumferentially.

Finally, the present data for the critical condition for the onset of the inertia-driven tertiary roll for $\Delta T \geqslant 5.0$ °C can be correlated empirically for $H = 10.0$ and 20.0 mm as

$$\ln\left[\frac{Gr}{Re_j^2} \times \left(\frac{D_j}{H}\right)\right] = -11.2 + 0.8\ln\left[Gr \times \left(\frac{D_j}{H}\right)\right]$$
$$- 0.65 \times \left(\frac{D_j}{H}\right)^{1.5} \quad (4)$$

and the onset of the quaternary rolls in the present chamber at $H = 10.0$ mm for $\Delta T \geqslant 5.0$ °C occurs at

$$Ra = -10,600 + 0.326Re_j^{1.5} \quad (5)$$

when compared with the present measured data, the standard deviations of the above two correlations are 3% and 9% individually.

3.2. Types of vortex flow instability

For the ranges of the parameters covered in the present study two types of vortex flow instability are identified in the experiment. At a sufficiently high jet Reynolds number beyond the critical Re_j for the onset of the secondary, tertiary or quaternary roll depending on the jet-to-disk separation distance, the vortex flow does not reach any steady state at long time and in fact it becomes time-dependent. This is an inertia-driven flow instability. On the other hand, the flow experiences another instability when the buoyancy predominates over the jet inertia at a high buoyancy-to-inertia ratio Gr/Re_j^2. Obviously, this is a buoyancy-driven flow instability. In the experiment the critical conditions for the onsets of these two instabilities are obtained by inspecting a number of video tapes recording the time evolution of the vortex flow patterns from the side and top views for given H and ΔT at a small step increase of 0.1 slpm for Q_j.

Besides, our data show that the buoyancy-driven instability exists in the flow for $H = 20.0$ mm at certain high the buoyancy-to-inertia ratio. For this intermediate H the inertia- and buoyancy-driven rolls do not contact and some free space between the two rolls is available for the new buoyancy-driven rolls to be induced at a high buoyancy-to-inertia ratio. These new rolls undergo growth, decay, disappearance and generation processes as the flow evolves. The characteristics of this buoyancy-driven time-dependent flow have been reported in the previous study [15]. For the smaller H of 10.0 mm the Rayleigh number tested here is not high enough to induce a buoyancy-driven flow instability. Only the inertia-driven flow instability exists. While for the large H of 30.0 mm the inertia-driven primary roll and the buoyancy-driven roll are in close contact and the resulting vortex flow instability is somewhat different. Both the increases in Re_j and/or Ra can induce vortex flow instability. It can be designated as a mixed vortex flow instability.

3.3. Time-dependent vortex flow

A close inspection of the inertia-driven time periodic vortex flow pattern shown in Fig. 4(a) reveals that for $H = 20.0$ mm at a supercritical Re_j above the onset of unsteady flow, relatively slight radial growth of the primary inertia-driven roll accompanying with slight decay of the secondary inertia-driven roll takes place in a certain period
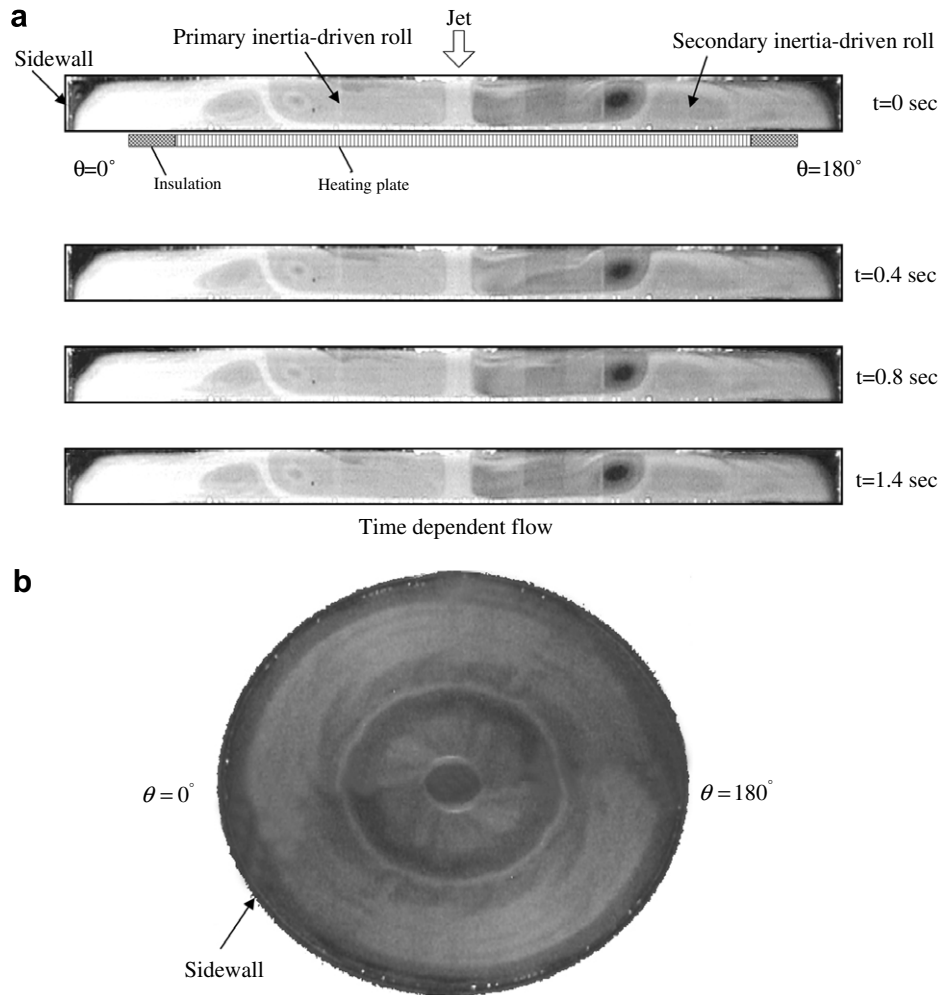
Fig. 4. Time periodic vortex flow for $H = 20.0$ mm and $Ra = 0$ ($\Delta T = 0$ °C) at $Re_j = 839$ ($Q_j = 6.2$ slpm) illustrated by (a) side view flow photos taken at the vertical plane $\theta = 0°$ and $\theta = 180°$ at selected time instants in a typical periodic cycle and (b) top view flow photo taken at middle horizontal plane halfway between the pipe exit and heated disk at certain time instant in the cycle ($t_p = 1.45$ s).

of time near the inter-boundary between the two rolls for $\Delta T = 0$ °C. In the subsequent period of time the reverse process occurs with the growth of the secondary roll and the decay of the primary roll. The flow is thus time-dependent. The deformed inter-boundary now can be more clearly seen from the top view flow photo (Fig. 4(b)). Moreover, at $H = 20.0$ the whole primary and secondary rolls are found to rotate circumferentially in the same direction. This circumferential rotation of the rolls is found to result from the high jet inertia associated with a high Re_j. It should be mentioned that in this figure and the figures to be presented the time $t = 0$ denotes certain time instant in the statistical state. At the high ΔT of 25.0 °C, Fig. 5 shows that the secondary inertia-driven roll merges with buoyancy-driven roll to form a big roll in the outer region of the chamber. This has been examined in our earlier study [15]. The slight cyclic growth and decay of the primary and the merged rolls around their inter-boundary are also seen for the case shown in Fig. 5 for a high Re_j. It should be mentioned that the time-dependent vortex flows shown in Figs. 4 and 5 are both slightly asymmetric.

As the jet-to-disk separation distance is increased to 30.0 mm, the time-dependent vortex flow is characterized by the growth of the primary inertia-driven roll accompanying with the squeezing of the buoyancy-driven roll in the first half of a typical period, followed with a reverse process in the second half of the period. At this higher H the circumferential rotation of the two rolls is more significant. These unique features of the unsteady flow are shown in Figs. 6 and 7 for selected Q_j and ΔT. Note that the time-dependent flow shown in Fig. 6 also exhibits slight asymmetry in the vortex rolls at this high buoyancy-to-inertia ratio. And the flow becomes more asymmetric for a higher Gr/Re_j^2 such as that presented in Fig. 7. Besides, at a higher Gr/Re_j^2 the rolls suffer from a more severe distortion. Note that the vortex flow pattern shown in Fig. 7 is like a polygon. The inner roll tends to break into a number of well-connected cells.

The characteristics of the time-dependent flow are further illustrated by examining the data from the transient temperature measurement. First, it is noted that at $H = 10.0$ and 20.0 mm the amplitude of the flow oscillation
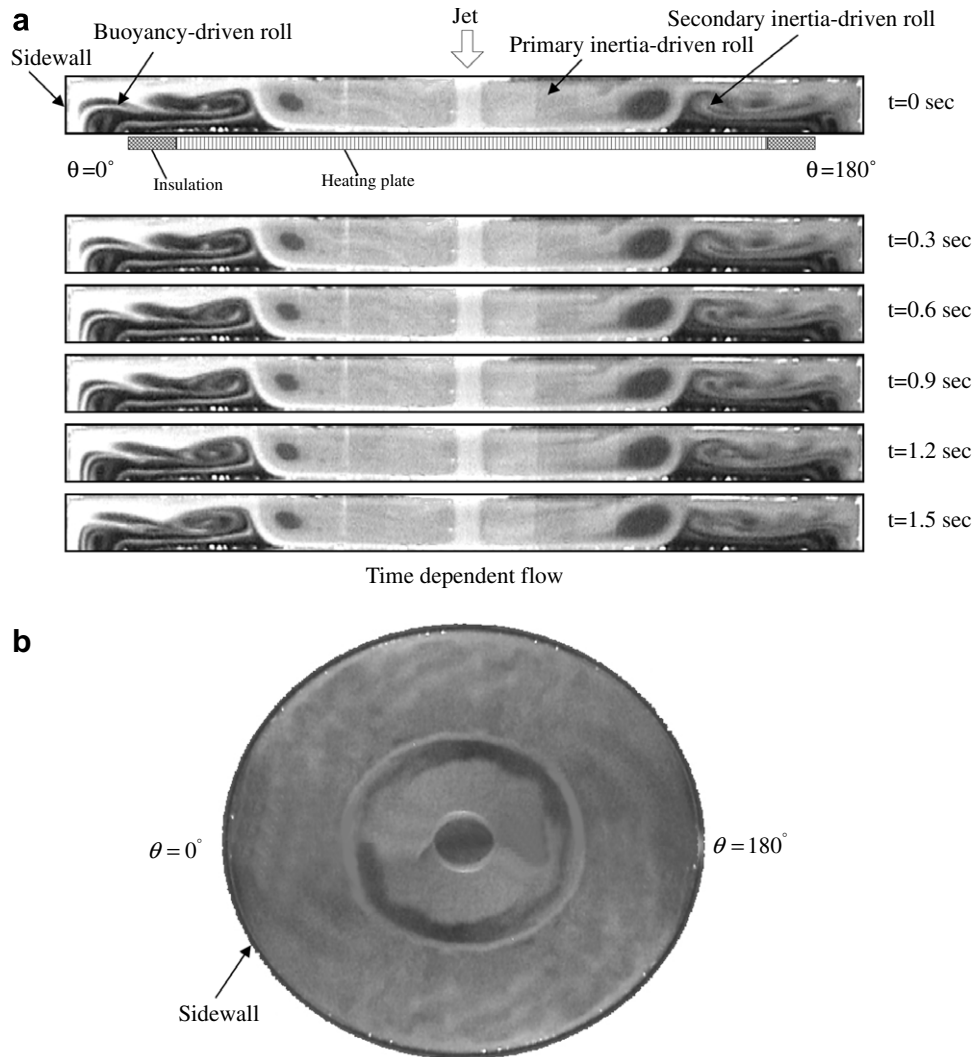
Fig. 5. Time periodic vortex flow for $H = 20.0$ mm and $Ra = 18,790$ ($\Delta T = 25.0$ °C) at $Re_j = 1028$ ($Q_j = 7.6$ slpm) illustrated by (a) side view flow photos taken at the vertical plane $\theta = 0°$ and $\theta = 180°$ at selected time instants in a typical periodic cycle and (b) top view flow photo taken at middle horizontal plane halfway between the pipe exit and heated disk at certain time instant in the cycle ($t_p = 1.58$ s).

in the inertia-driven time-dependent flow for the range of supercritical Re_j covered in this study is small. Hence the temperature oscillation in the flow is also very small and in fact it is at the same order of magnitude as the background disturbances. But for the large H of 30.0 mm the temperature oscillation can be significant. The time records of the non-dimensional air temperature Φ defined as $(T - T_j)/(T_f - T_j)$ at selected locations for the case with $Re_j = 676$ and $Ra = 63,420$ are shown in Fig. 8. Note that the amplitude of the temperature oscillation varies substantially with the locations. More specifically, in the upper region of the chamber the air temperature oscillates in a larger amplitude (Fig. 8(c)), except in the side wall region. Elsewhere in the lower half of the chamber the temperature oscillation is rather small and its amplitude is very close to the background disturbances (Fig. 8(a) and (b)). Moreover, the results given in Fig. 9 show that the frequency of the temperature oscillation is affected by both the jet Reynolds and Rayleigh numbers. The Rayleigh number exhibits a

milder effect. However, the oscillation frequency increases significantly with Re_j. The corresponding evolutions of the time periodic flow in a typical periodic cycle for selected cases are already illustrated in Figs. 6 and 7 for $H = 30.0$ mm. The mutual pushing and squeezing of the two rolls in the chamber are clearly seen. The size change of the rolls with time is noticeable according to the side view flow photos. Moreover, the mutual interaction of the rolls causes the vortex flow inside the rolls to become somewhat irregular, as evident from the top view flow photos. This vortex flow irregularity is more pronounced at a higher buoyancy-to-inertia ratio.

3.4. Reverse flow transition at increasing buoyancy

Finally, the effects of the Rayleigh number on the inertia-driven time-dependent flow require some further discussion. It is known from Table 2 that for the small H of 10.0 and 20.0 mm the critical Re_j for the onset of the
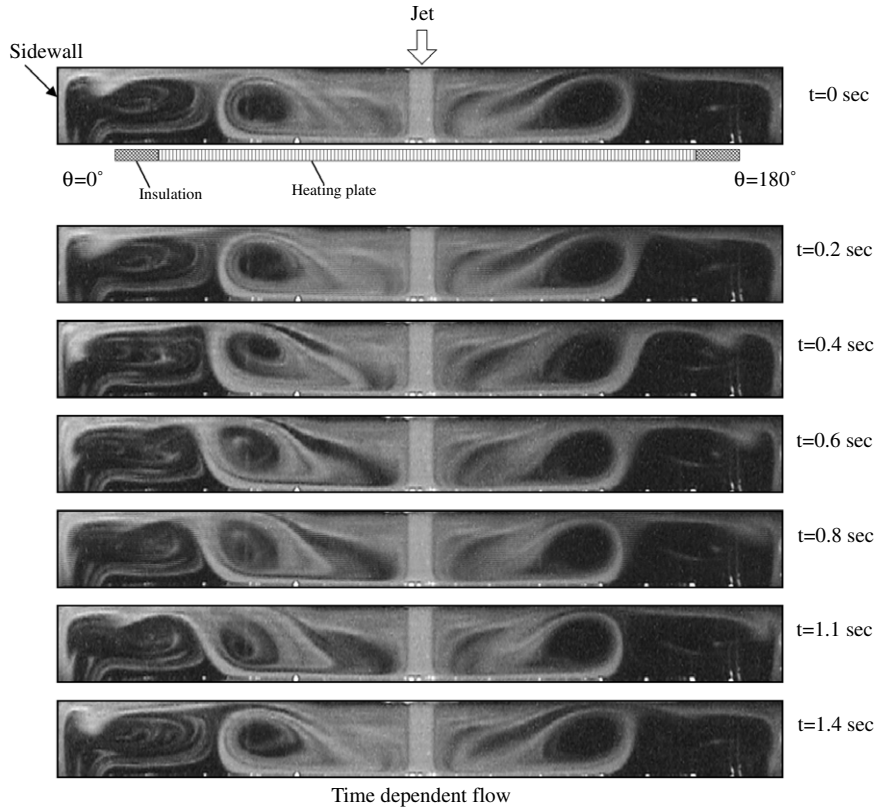
Fig. 6. Time periodic vortex flow for $H = 30.0$ mm and $Ra = 63,420$ ($\Delta T = 25.0$ °C) at $Re_j = 676$ ($Q_j = 5.0$ slpm) illustrated by side view flow photos taken at the vertical plane $\theta = 0°$ and $\theta = 180°$ at selected time instants in a typical periodic cycle ($t_p = 1.43$ s).

inertia-driven time-dependent flow is higher for a higher ΔT. This suggests that an increase in ΔT can stabilize the inertia-driven time-dependent flow. It is important to elucidate why the inertia-driven time-dependent flow can be stabilized by raising the ΔT. A close inspection of the vortex flow at supercritical Re_j for various ΔT for $H = 10.0$ and 20.0 mm reveals that the buoyancy-driven roll is bigger and stronger at increasing ΔT. As the buoyancy-driven roll grows to a certain large size, it merges with the secondary inertia-driven roll and the larger merged roll is in close contact with the inertia-driven rolls and can retard the oscillation of the inertia-driven rolls. Thus the time-dependent flow is stabilized. The results show that at $\Delta T = 0$ and 5.0 °C the flow is time periodic at certain high Re_j. But at the higher $\Delta T \geqslant 10.0$ °C steady flow prevails in the chamber at the same Re_j. Thus we have a reverse flow transition at increasing buoyancy. Next, an opposite trend is noted for the large H of 30.0 mm (Table 2). At this high H both the inertia- and buoyancy-driven rolls are relatively large for given Re_j and ΔT ($\geqslant 5.0$ °C). An increase in ΔT causes the buoyancy-driven roll to push and squeeze the inertia-driven roll. The inertia-driven roll then pushes back and initiates the flow unsteadiness.

3.5. Flow regime maps

Based on the present data, the flow regime maps delineating the temporal state of the inertia- and buoyancy-dri-

ven flow in the processing chamber are provided in Figs. 10 and 11 for $H = 20.0$ and 30.0 mm. Note that at $H = 20.0$ mm both the inertia- and buoyancy-driven vortex flow instabilities take place. The buoyancy-driven unstable flow appears at very high buoyancy-to-inertia ratio (Fig. 10). The boundary separating the non-periodic buoyancy-induced vortex flow and the time periodic buoyancy-induced unstable vortex flow for $H = 20.0$ mm can be empirically correlated as

$$Ra = 10,800 + 0.0568Re_j^2$$
$$\text{for } 7520 \leqslant Ra \leqslant 18,790 \text{ and } 189 \leqslant Re_j \leqslant 379 \quad (6)$$

The boundary between the stable vortex flow and the time periodic buoyancy-driven vortex flow for $H = 20.0$ mm can be correlated as

$$Ra = 4160 + 0.1Re_j^2$$
$$\text{for } 11,270 \leqslant Ra \leqslant 15,030 \text{ and } 108 \leqslant Re_j \leqslant 250 \quad (7)$$

The transition from the stable vortex flow to the time periodic inertia-driven vortex flow occurs at

$$Ra = -74,300 + 92.6Re_j$$
$$\text{for } 0 \leqslant Ra \leqslant 18,790 \text{ and } 798 \leqslant Re_j \leqslant 987 \quad (8)$$

The boundary between the time periodic inertia-driven vortex flow and the non-periodic inertia-driven vortex flow can be correlated as
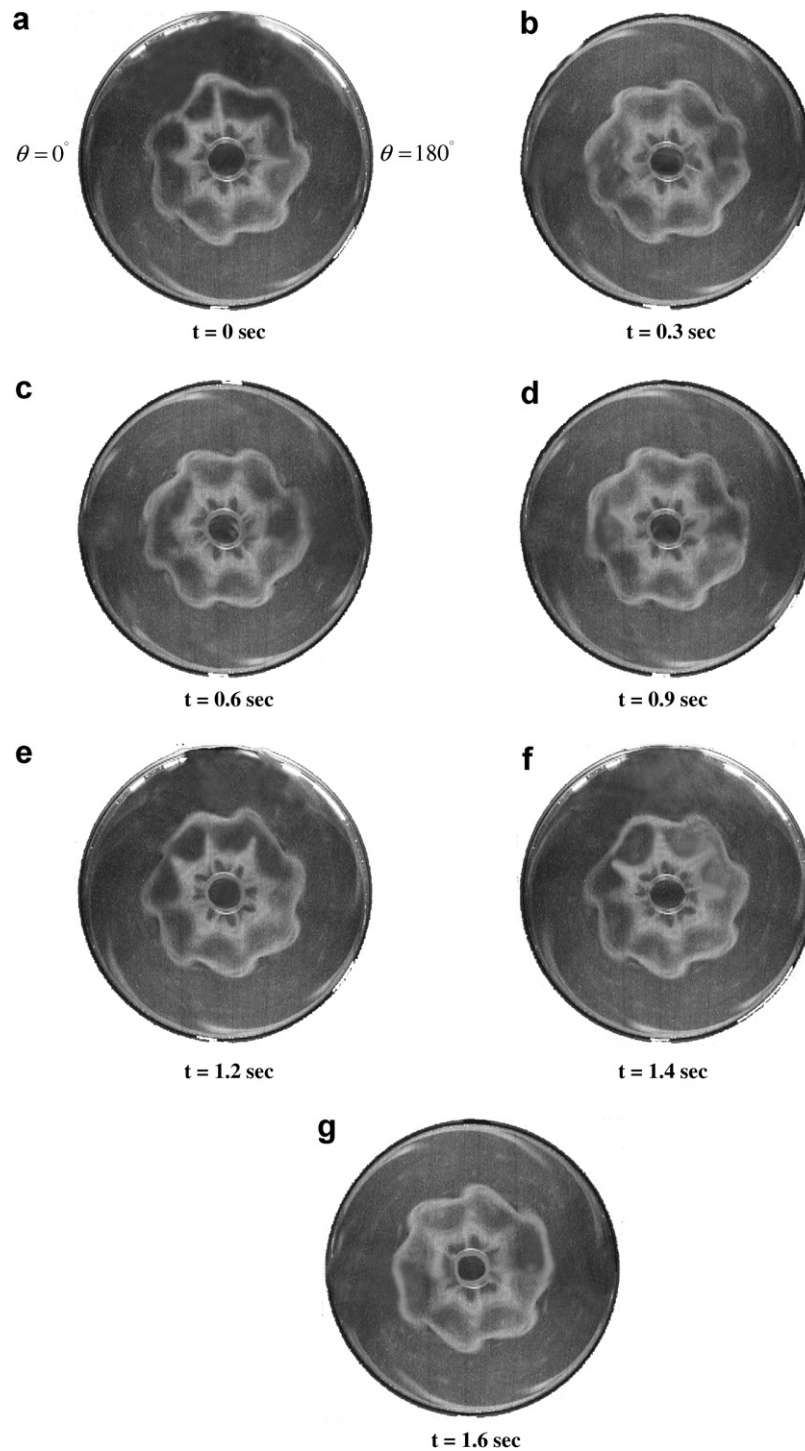
Fig. 7. Top view flow photos taken at selected time instants in a typical periodic cycle with $Ra = 63{,}420$ ($\Delta T = 25.0\ °C$), $Q = 4.0$ slpm ($Re_j = 541$) and $H = 30.0$ mm ($t_p = 1.67$ s).

$$Ra = -120{,}000 + 111.0Re_j$$
$$\text{for } 0 \leqslant Ra \leqslant 18{,}790 \text{ and } 1082 \leqslant Re_j \leqslant 1258 \quad (9)$$

These four correlations are also indicated in Fig. 10.

Then, the transition from the stable vortex flow to the time periodic vortex flow for $H = 30.0$ mm occurs at

$$Ra = 102{,}000 - 0.149Re_j^2$$
$$\text{for } 0 \leqslant Ra \leqslant 63{,}420 \text{ and } 473 \leqslant Re_j \leqslant 788 \quad (10)$$

The boundary between the time periodic vortex flow and the non-periodic vortex flow can be correlated as

$$Ra = 269{,}000 - 224.0Re_j,$$
$$\text{for } 0 \leqslant Ra \leqslant 63{,}420 \text{ and } 947 \leqslant Re_j \leqslant 1204 \quad (11)$$

These two correlations are also shown in Fig. 11.

Finally, it is clearly noted from the instability boundaries shown in Figs. 10 and 11 that the inertia-driven unstable
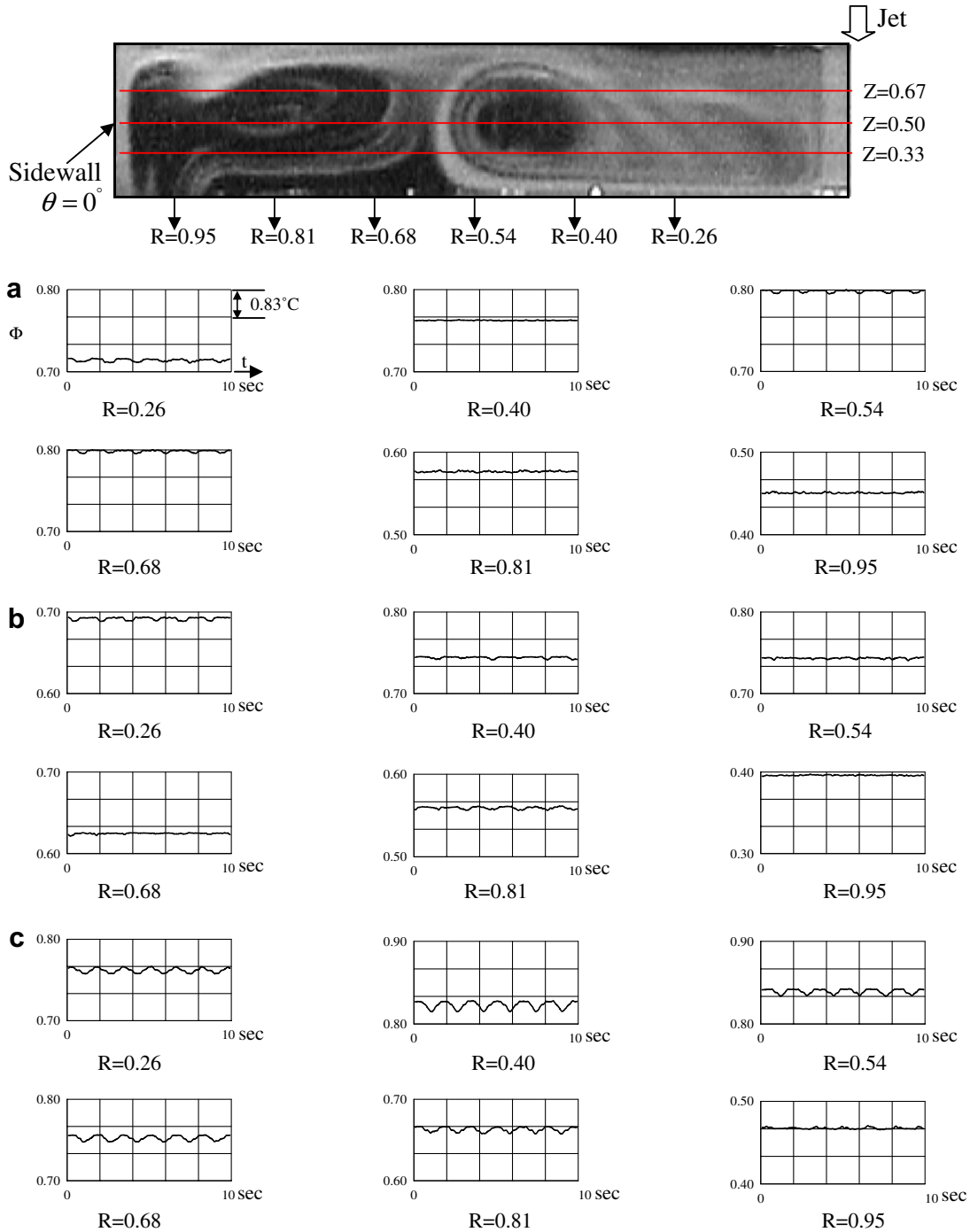
Fig. 8. The time records of non-dimensional air temperature for $Ra = 63,420$ ($\Delta T = 25.0$ °C) and $Re_j = 676$ ($Q_j = 5.0$ slpm) with $H = 30.0$ mm at selected locations for (a) $Z = 0.33$, (b) $Z = 0.50$, and (c) $Z = 0.67$ on the cross plane $\theta = 0°$ ($t_p = 1.43$ s).

flow at certain high Re_j for $H = 20.0$ mm can be stabilized by increasing the buoyancy (ΔT). However, for $H = 30.0$ mm a stable flow prevailed at low Re_j can be destabilized by an increase in ΔT due to the decrease of the critical Re_j at increasing ΔT (Fig. 11). We further note the simultaneous presence of the buoyancy- and inertia-driven flow instability in the chamber with $H = 20.0$ mm. Thus for $H = 20.0$ mm and at a certain high ΔT the vortex flow

can be time dependent at low Re_j resulting from the buoyancy-driven instability. For Re_j raised to some intermediate level, the buoyancy-to-inertia ratio is lower and the vortex flow is stable. But for a further increase of Re_j to a certain high level, the inertia-driven flow instability sets in and the flow becomes unstable. Hence for $H = 20.0$ mm the vortex flow experiences a reverse flow transition at increasing Re_j, as mentioned in the previous section.
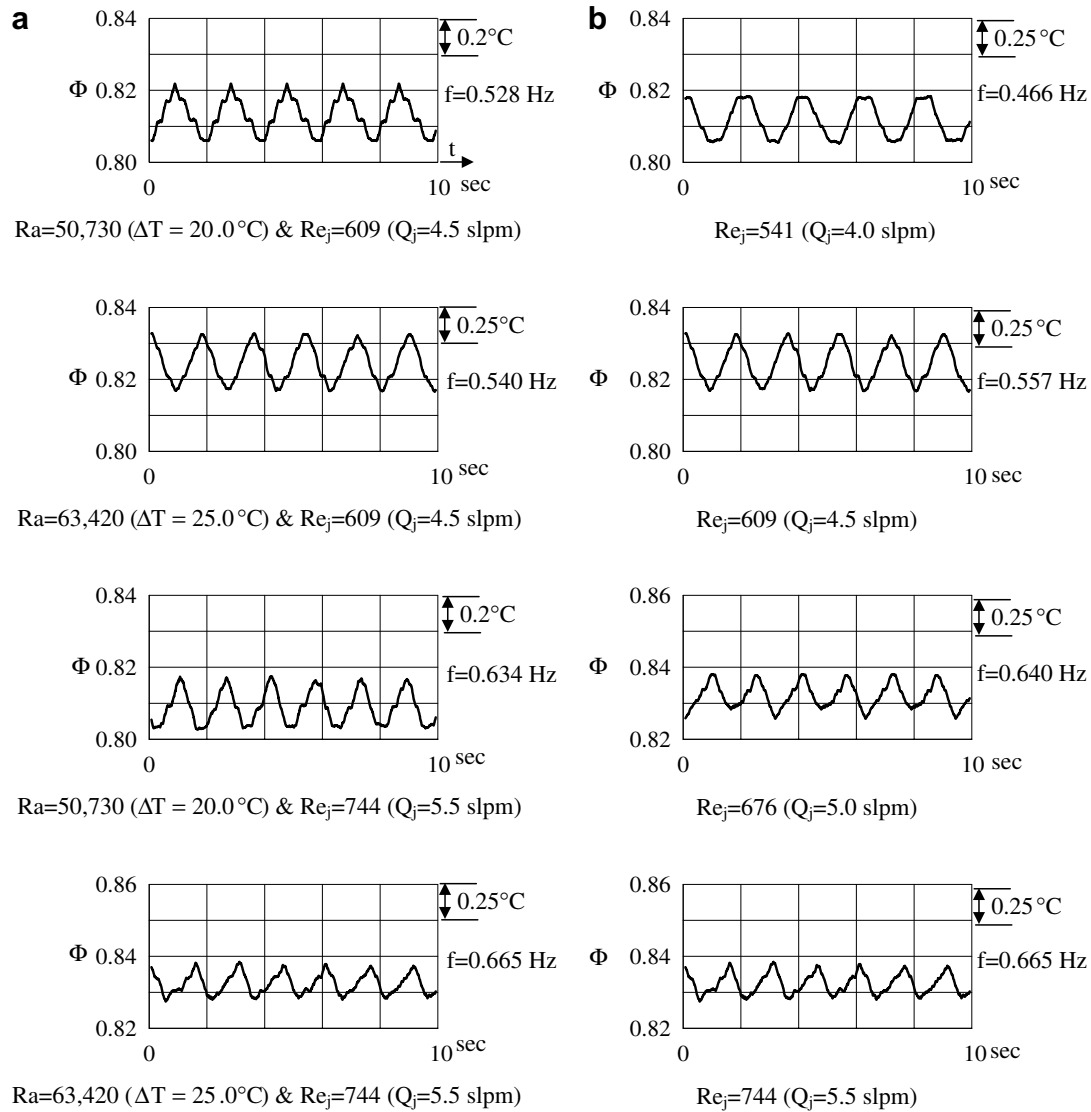
Fig. 9. The time records of non-dimensional air temperature with $H = 30.0$ mm at location $(R, Z) = (0.58, 0.67)$ on the vertical plane $\theta = 0°$ for (a) various Rayleigh numbers at fixed Reynolds number and (b) various Reynolds numbers at $Ra = 63,420$.

4. Concluding remarks

An experiment combining flow visualization and temperature measurement is conducted in the present study to explore the possible presence of new inertia-driven vortex rolls and some unique time-dependent vortex flow characteristics associated with an air jet impinging onto a horizontal circular heated disk confined in a vertical cylindrical chamber. Effects of the inlet gas flow rate, temperature difference between the heated disk and cold air jet, and the jet-to-disk separation distance on the unique vortex flow characteristics are inspected in detail. The major results obtained in the present study can be briefly summarized in the following.

(1) The critical Re_j for the onset of the tertiary and quaternary inertia-driven vortex rolls are higher at increasing temperature difference between the heated plate and injection air for $H = 10.0$ and 20.0 mm.

(2) The onset of the inertia-driven time-dependent vortex flow occurs at higher Re_j than that for the onset of tertiary and quaternary rolls. This critical Re_j increases with ΔT for $H = 10.0$ and 20.0 mm. But the opposite is true for $H = 30.0$ mm. In the time-dependent flow the vortex rolls deform noticeably and the flow pattern is like a polygon. The inner roll tends to break into a number of well-connected cells. Moreover, the deformed vortex rolls slowly rotate in the circumferential direction.

(3) For $H = 20.0$ mm both the inertia- and buoyancy-driven flow instabilities exist and reverse flow transition can appear at increasing Re_j.

During the course of this investigation, it has been realized that the new inertia-driven vortex rolls and some unique characteristics of the time-dependent mixed convective vortex flow in a round air jet impinging onto a heated
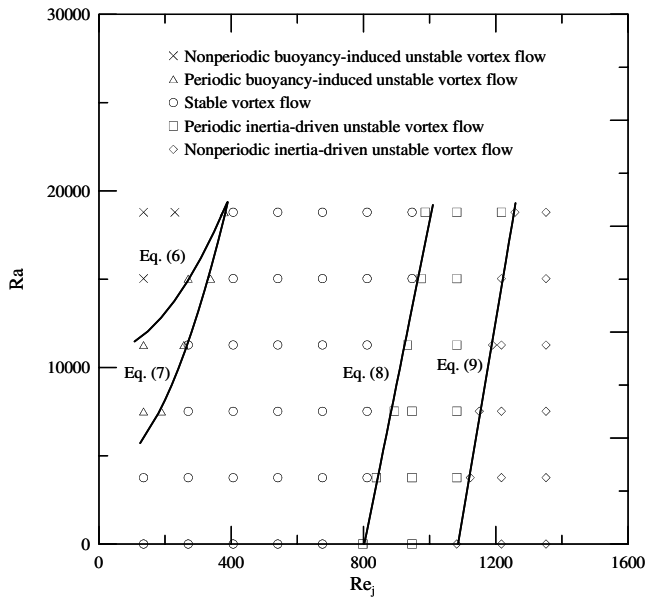
Fig. 10. Flow regime map delineating the temporal state of the vortex flow for $H = 20.0$ mm.
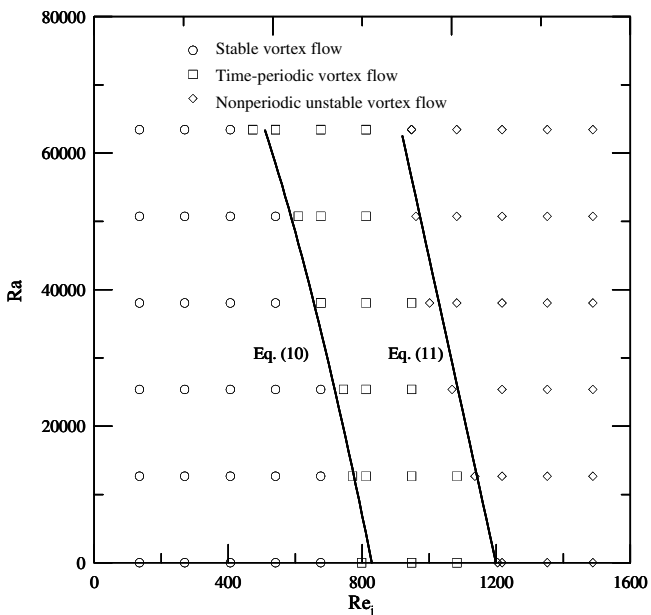

Fig. 11. Flow regime map delineating the temporal state of the vortex flow for $H = 30.0$ mm.

horizontal circular disk in a vertical cylindrical chamber can be significantly affected by the Reynolds and Rayleigh numbers. Moreover, the disk rotation is expected to greatly affect the structures of the vortex flow. Some flow stabilization may be obtained. These will be explored in the near future.

Acknowledgement

References

[1] J.R. Guarino, V.P. Manno, Characterization of laminar jet impinge-ment cooling in portable computer applications, IEEE Trans. Compon. Pack. Technol. 25 (2002) 337–346.

[2] S.A. Campbell, The Science and Engineering of Microelectronic Fabrication, Oxford University Press, New York, 1996 (Chapter 6).

[3] M.L. Hitchamn, K.F. Jensen, Chemical Vapor Deposition (Principle and Application), Academic Press, San Diego, 1993 (Chapter 2).

[4] M.T. Scholtz, O. Trass, Mass transfer in a nonuniform impinging jet, AIChE J. 16 (1970) 82–96.

[5] E.M. Sparrow, T.C. Wong, Impingement transfer coefficients due to initially laminar slot jets, Int. J. Heat Mass Transfer 18 (1975) 597–605.

[6] J.H. Masliyah, T.T. Nguyen, Mass transfer due to an impinging slot jet, Int. J. Heat Mass Transfer 22 (1979) 237–244.

[7] P. Hrycak, Heat transfer from round impinging jets to a flat plate, Int. J. Heat Mass Transfer 26 (1981) 1857–1865.

[8] N.R. Saad, W.J.M. Douglas, A.S. Mujumdar, Prediction of heat transfer under an axisymmetric laminar impinging jet, Ind. Eng. Chem. Fundam. 16 (1977) 148–154.

[9] H.S. Law, J.H. Masliyah, Mass transfer due to a confined laminar impinging axisymmetric jet, Ind. Eng. Chem. Fundam. 23 (1984) 446–454.

[10] L.P. Chua, S.C.M. Yu, H-S. Li, Flow visualization and preliminary measurements of a confined jet with and without target, Int. Commun. Heat Mass Transfer 27 (2000) 191–200.

[11] P.R. Voke, S. Gao, Numerical study of heat transfer from an impinging jet, Int. J. Heat Mass Transfer 41 (1998) 671–680.

[12] H.V. Santen, C.R. Kleijn, H.E.A. Van Den Akker, Mixed convection in radial flow between horizontal plates—I. Numerical simulations, Int. J. Heat Mass Transfer 43 (2000) 1523–1535.

[13] H.V. Santen, C.R. Kleijn, H.E.A. Van Den Akker, Mixed convection in radial flow between horizontal plates—II. Experiments, Int. J. Heat Mass Transfer 43 (2000) 1537–1546.

[14] T.C. Cheng, P.H. Chiou, T.F. Lin, Visualization of mixed convective vortex rolls in an impinging jet flow of air through a cylindrical chamber, Int. J. Heat Mass Transfer 45 (2002) 3357–3368.

[15] J.C. Hsieh, T.C. Cheng, T.F. Lin, Characteristics of vortex flow in a low speed air jet impinging onto a heated disk in a vertical cylindrical chamber, Int. J. Heat Mass Transfer 46 (2003) 4639–4656.

[16] Y.M. Chung, K.H. Luo, Unsteady heat transfer analysis of an impinging jet, J. Heat Transfer 124 (2002) 1039–1048.

[17] V.A. Chiriac, A. Ortega, A numerical study of the unsteady flow and heat transfer in a transitional confined slot jet impinging on an isothermal surface, Int. J. Heat Mass Transfer 45 (2002) 1237–1248.

[18] B. Elison, B.W. Webb, Local heat transfer to impinging liquid jets in the initially laminar transitional and turbulent regimes, Int. J. Heat Mass Transfer 37 (1994) 1027–1216.

[19] V. Narayanan, J. Seyed-Yagoobi, R.H. Page, An experimental study of fluid mechanics and heat transfer in an impinging slot jet flow, Int. J. Heat Mass Transfer 47 (2004) 1827–1845.

[20] R. Viskanta, Heat transfer to impinging isothermal gas and flame jets, Exp. Therm. Fluid Sci. 6 (1993) 111–134.

[21] K. Jambunathan, E. Lai, M.A. Moss, B.L. Button, A review of heat transfer data for single circular jet impingement, Int. J. Heat Fluid Flow 13 (1992) 106–115.

[22] J.C. Hsieh, T.F. Lin, Effects of jet-to-disk separation distance on the characteristics of mixed convective vortex flow in an impinging air jet confined in a cylindrical chamber, Int. J. Heat Mass Transfer 48 (2005) 511–525.

[23] S.J. Kline, F.A. McClintock, Describing uncertainties in single-sample experiment, Mech. Eng. 75 (1953) 3–8.